Propagation of the Storegga tsunami in the southeastern North Sea

By:

Steven J. Gibbons steven.gibbons@ngi.no (https://orcid.org/0000-0002-7822-0244)
Stein Bondevik Stein.Bondevik@hvl.no (https://orcid.org/0000-0003-0114-6901)
Bartosz Kurjanski bkurjanski@abdn.ac.uk (https://orcid.org/0000-0001-8797-6425)
Marc de la Asunción marcah@uma.es (https://orcid.org/0000-0003-3130-1335)
Valentina Magni valentina.magni@ngi.no (https://orcid.org/0000-0003-2882-1954)
Jorge Macías Sánchez jmacias@uma.es (https://orcid.org/0000-0002-3010-8050)
Andy R. Emery A.Emery@wessexarch.co.uk (https://orcid.org/0000-0003-1231-0148)
Finn Løvholt Finn.Lovholt@ngi.no (https://orcid.org/0000-0003-1019-7321)

Postprint of unedited version of manuscript submitted to **Quaternary Science Advances**, 18 June 2026. Final version published on https://doi.org/10.1016/j.qsa.2026.100345
25 September 2026.

Keywords:
Storegga, Landslide, Tsunami, Dogger Bank, North Sea, Numerical simulations

Abstract:

Numerical simulations of the 8150 BP Storegga slide event in the Norwegian Sea are necessary for understanding both landslide dynamics and tsunami propagation. Here we focus on the southern North Sea, South East of Dogger Bank, and the shores of Denmark and Germany where there have been reports of Storegga tsunami deposits. We simulate the slide using a recently developed cohesive landslide model that has demonstrated success in predicting both the extent of landslide run-out and tsunami run-up heights farther north, and we model sea surface elevations, current velocities, and arrival times of the tsunami. However, the model results rely on using an accurate bathymetry for 8150 years ago, but for this part of the southern North Sea such a palaeobathymetry is somewhat uncertain. Thus, we parametrize a continuum of bathymetric models between the present-day bathymetry through two different palaeobathymetric models, and then perform complete simulations for multiple candidate bathymetric models. For many models in which Dogger Bank is completely submerged, the shallow water in this part of the North Sea still represents a significant barrier to tsunami propagation. We compare tsunami metrics between the alternative bathymetries systematically and conclude that the tsunami surface elevations and velocities in the southeastern North Sea are probably too small to have caused erosion and significant deposition of tsunami debris along the coasts of Denmark and Germany. Instead, we reinterpret the deposits as related to the inundation of the coast during the Holocene sea level rise between 7000 and 8000 years ago.

Postprint of pre-publication version.
Final version found on https://doi.org/10.1016/j.qsa.2026.100345

Highlights

Propagation of the Storegga tsunami in the southeastern North Sea

Steven J. Gibbons, Stein Bondevik, Bartosz Kurjanski, Marc de la Asunción, Valentina Magni, Jorge Macías Sánchez, Andy R. Emery, Finn Løvholt

- We have simulated the Storegga slide and tsunami 8150 years ago in the Norwegian Sea and North Sea.
- We map out metrics of tsunami intensity for the present-day North Sea and for the much shallower North Sea 8150 years ago.
- South East of Doggerland in the 8150 BP simulations, the wave propagates far slower and with greatly reduced amplitudes.
- From the simulations, it appears unlikely that the Storegga tsunami could leave traces in present-day Germany and southern Denmark.
- We suggest that claimed Storegga tsunami deposits in Denmark and Germany instead are the result of the Holocene transgression that inundated these coastlines 7000-8000 cal year BP.

Propagation of the Storegga tsunami in the southeastern North Sea

Steven J. Gibbons[a,*], Stein Bondevik[b], Bartosz Kurjanski[c], Marc de la Asunción[d], Valentina Magni[a], Jorge Macías Sánchez[d], Andy R. Emery[c,e] and Finn Løvholt[a]

[a]*Norges Geotekniske Institute, Sandakerveien 140, 0484 Oslo, Norway*
[b]*Department of Civil Engineering and Environmental Sciences, Høgskulen på Vestlandet, N-6851 Sogndal, Norway*
[c]*Department of Geology and Geophysics, University of Aberdeen, Aberdeen, United Kingdom*
[d]*Departamento de Análisis Matemático, Estadística e Investigación Operativa, y Matemática Aplicada, Universidad de Málaga, Málaga, Spain*
[e]*Wessex Archaeology, Edinburgh, United Kingdom*

ARTICLE INFO

Keywords:
Storegga
landslide
tsunami
Dogger Bank
North Sea
Numerical simulation

ABSTRACT

Numerical simulations of the 8150 BP Storegga slide event in the Norwegian Sea are necessary for understanding both landslide dynamics and tsunami propagation. Here we focus on the southern North Sea, South East of Dogger Bank, and the shores of Denmark and Germany where there have been reports of Storegga tsunami deposits. We simulate the slide using a recently developed cohesive landslide model that has demonstrated success in predicting both the extent of landslide run-out and tsunami run-up heights farther north, and we model sea surface elevations, current velocities, and arrival times of the tsunami. However, the model results rely on using an accurate bathymetry for 8150 years ago, but for this part of the southern North Sea such a palaeobathymetry is somewhat uncertain. Thus, we parametrize a continuum of bathymetric models between the present-day bathymetry through two different palaeobathymetric models, and then perform complete simulations for multiple candidate bathymetric models. For many models in which Dogger Bank is completely submerged, the shallow water in this part of the North Sea still represents a significant barrier to tsunami propagation. We compare tsunami metrics between the alternative bathymetries systematically and conclude that the tsunami surface elevations and velocities in the southeastern North Sea are probably too small to have caused erosion and significant deposition of tsunami debris along the coasts of Denmark and Germany. Instead, we reinterpret the deposits as related to the inundation of the coast during the Holocene sea level rise between 7000 and 8000 years ago.

Introduction

The Storegga Slide (Bugge et al., 1988; Bryn et al., 2005), off the northwestern coast of Norway, around 8150 cal BP, is one of the largest landslides recorded globally in recent geological time. It resulted in a tsunami that impacted coasts around the North Atlantic with run-up greatly exceeding 10 m on the nearest coastlines including, among others, the coastlines of Norway, Shetland, the Faroes, and Scotland (e.g. Bondevik et al., 1997a, 2003; Løvholt et al., 2017). The event is evidenced both in onshore tsunami deposits (e.g. Bondevik et al., 1997b) and in slide debris downslope of the slide scar (e.g. Haflidason et al., 2004, 2005), as well as a turbidity current deposited over a wider area. Although interpretations of the Storegga Slide conclude that the landslide evolved in separate stages (e.g. Bugge et al., 1988;

*Corresponding author
steven.gibbons@ngi.no (S.J. Gibbons); stein.bondevik@hvl.no (S. Bondevik); bkurjanski@abdn.ac.uk (B. Kurjanski); marcah@uma.es (M.d.l. Asunción); valentina.magni@ngi.no (V. Magni); jmacias@uma.es (J.M. Sánchez); A.Emery@wessexarch.co.uk (A.R. Emery); finn.lovholt@ngi.no (F. Løvholt)
ORCID(s): 0000-0002-7822-0244 (S.J. Gibbons); 0000-0003-0114-6901 (S. Bondevik); 0000-0001-8797-6425 (B. Kurjanski); 0000-0003-3130-1335 (M.d.l. Asunción); 0000-0003-2882-1954 (V. Magni); 0000-0002-3010-8050 (J.M. Sánchez); 0000-0003-1231-0148 (A.R. Emery); 0000-0003-1019-7321 (F. Løvholt)

Karstens et al., 2023), it seems likely that the greatest part of the landslide volume was emplaced in a single event involving retrogressive failure (e.g. Bryn et al., 2005; Kvalstad et al., 2005).

A key aspect for understanding the emplacement process is obtained by modelling the landslide dynamics, and tsunami generation and propagation. Since the early nineties, our understanding of the event has gradually been refined through multiple studies (e.g. Harbitz, 1992; Bondevik et al., 2005; Hill et al., 2014; Løvholt et al., 2017; Kim et al., 2019). Among others, recent studies matching both the landslide run-out distance and the palaeotsunami observations (Løvholt et al., 2017; Kim et al., 2019) confirmed that the most of the landslide volume must have failed within a short amount of time to be sufficiently efficient to generate the tsunami, implying that the duration of the retrogressive failure process must have been short, even if crucial for the initiation phase, and evident for the last phase (Gauer et al., 2005). While some of these studies have focused mainly on reproducing tsunami observations in Norway, Shetland, the Faroe Islands, and Scotland, a key remaining question is whether or not the tsunami inundated coastlines further south in the North Sea to a substantial degree.

Accurate models of tsunami characteristics are important for validating or dismissing observations in various locations (e.g. Earland et al., 2024; Devendra et al., 2025) and, for example, assessing the potential impacts on Mesolithic communities (e.g. Rydgren and Bondevik, 2015; Walker et al., 2024). On the basis of numerical simulations, and detailed re-investigation of a sediment core, Bondevik et al. (2024) demonstrated that marine deposits that had been associated with the 8200-year BP cooling event were reworked by Storegga tsunami currents on the sea floor in the Norwegian Sea. Tsunami generation and propagation is sensitive to both the landslide dynamics and the water depth of tsunami generation, implying that the tsunami observations can be considered a footprint of the landslide motion, where the first failure phase and the landslide acceleration is of most importance for the tsunami generation (Løvholt et al., 2005; Harbitz et al., 2006; Løvholt et al., 2015).

The ability of the tsunami to leave evidence in the sedimentary record at a given location is contingent on a bathymetry that facilitates propagation to that shoreline. The coastline and bathymetry of the North Sea have changed in response to unloading of the crust by melting ice sheets (glacio-isostatic adjustment; GIA), as well as sea level rise due to the release of water stored in ice into the global ocean (Fig. 1). Along the coastlines of the northern North Sea, the relative sea level (RSL) fell and continues to fall, whereas in the present day southern North Sea, which was mostly terrestrial following deglaciation, the land has been gradually drowned following the Last Glacial Maximum (LGM, e.g. Lambeck et al., 1998; Clark et al., 2012; Emery et al., 2020). At the time of Storegga, c. 8150 cal BP, the southern North Sea was far shallower than today. The shallow Dogger Bank located between UK and Denmark, at that time was either partially terrestrially exposed on the western side or submerged in very shallow waters (1-5m) in each case forming a shallow bathymetric bank: a likely barrier to tsunami wave propagation. Water depths further north in the central and northern North Sea were either similar to or greater than at present.

We stress that the sensitivity of tsunami propagation to absolute differences in the water depth are greater in shallow water than in deep water. Consequently, the water depths of the southeastern limits of the North Sea are crucial in the ability to explain the presence or genesis of any sediments resulting from Storegga in northern Germany or the west coast of Denmark as presented by Fruergaard et al. (2015b) and, more recently, Vött et al. (2024) (Fig. 1). Hill et al. (2014) compared the simulated propagation of a tsunami resulting from a model of the Storegga slide on contemporary bathymetry and a palaeobathymetric model in which parts of Dogger Bank were above sea level and in which the southeastern North Sea was significantly shallower than today. The wave height modelled by Hill et al. (2014) using the palaeobathymetry was significantly lower south of Dogger Bank than that modelled using the contemporary bathymetry.

In this study we seek to reassess the properties of the Storegga tsunami in the southeastern North Sea using two recent palaeobathymetric models of the North Sea for 8 ka BP as input. The most recent model we apply is that sourced from Clark et al. (2022b), displayed in Fig. 1 together with the present-day bathymetry. (Details of this palaeobathymetric model are subsequently elaborated in Bradley et al., 2023). We also use the model applied in Hill et al. (2014), which can be traced back to Bradley et al. (2011). Almost all of the results displayed in this paper were calculated using the model of Clark et al. (2022b), although the results from all of the simulations are made available online. The two palaeo-models differ in fine detail but are similar to first order. The area of greatest interest to us in this study, south-east of Dogger Bank, is similar in the two models: in particular with regard to the extent of land off the coasts of present day Denmark and Germany. This area was not covered by the Eurasian ice sheet complex (Houmark-Nielsen, 2004; Clark et al., 2022b; Patton et al., 2017; Shennan et al., 2018). Aware of uncertainties surrounding the palaeobathymetry, we define two families of models stretching between the present-day topobathymetry and each of the two palaeobathymetries applied to test the sensitivity of tsunami propagation to the imposed depth function. We perform tsunami simulations on each of these hypothetical topobathymetric models to understand the possible range of outcomes.

We seek also to demonstrate convergence of the tsunami model with respect to spatial resolution, with a particular focus on propagation in shallow areas. We display metrics of the tsunami simulation - maximum surface elevation, arrival time, maximum modulus of velocity (hereafter called flow speed) - in order to assess the likely impact of the tsunami in the southeastern North Sea. Fig. 1 displays not only the greater extent of terrestrially exposed land estimated in the south-east North Sea region around the time of Storegga but also the qualitatively different morphology of the seafloor. We simulate the landslide dynamics using the BingCLAW model (Løvholt et al., 2017; Kim et al., 2019), a depth-averaged model for a cohesive type Herschel-Bulkley fluid that is well suited for modelling clay rich cohesive fluids such as Storegga. In the present study, we apply the set of landslide rheological parameters for the BingCLAW simulation that Kim et al. (2019) found to provide the best match for both run-out and tsunami heights. For modelling the Storegga Slide and tsunami, the landslide model has also been applied in a number of recent studies examining inundation at sites along the Norwegian coastline (Walker et al., 2024), surface elevations and velocities at key core sites (Bondevik et al., 2024), and wave propagation into the high Arctic (Devendra et al., 2025).

Section 1 presents details of the numerical model for both landslide and tsunami. Section 2 presents and compares observations of fundamental tsunami metrics as a function of location for simulations on both contemporary and palaeobathymetries. We demonstrate convergence of the numerical results as the simulation resolution becomes finer. Section 3 investigates the sensitivity of tsunami characteristics in the south-eastern North Sea to the imposed topobathymetry by considering a continuum of bathymetric models spanning between the present day topobathymetry and each of two different palaeobathymetric models. In this way, we address the inherent uncertainties relating to palaeobathymetric reconstructions. We finally discuss the likely consequences.

1. The numerical model

The landslide and tsunami simulations are performed separately and sequentially, using respectively the BingCLAW and Tsunami-HySEA codes. BingCLAW landslide simulations have previously been applied to cases such as the Grand Banks tsunami (Løvholt et al., 2019), the Rissa quick clay slide and tsunami (Liu et al., 2021), dam break tests (Vanneste et al., 2019), and run-out sensitivity studies (Zengaffinen-Morris et al., 2022). Output from BingCLAW has been coupled to different tsunami simulation codes. The study of Kim et al. (2019) applied the shallow water Geoclaw code (Berger et al., 2011; Leveque et al., 2011) whereas the more recent studies for Storegga discussed above used the Boussinesq type GloBouss model (Løvholt et al., 2008, 2010). The Tsunami-HySEA model (de la Asunción et al., 2013) has been extensively tested and optimized for High Performance Computing under the Center of Excellence for Exascale in the Solid Earth (ChEESE) project (Folch et al., 2023). Tsunami-HySEA has been extensively benchmarked for both earthquake and landslide sources (e.g. Macías et al., 2017, 2020a,b, 2021). We stress that because of the long wavelength-to-depth ratios involved in the generation of the Storegga Slide tsunami, the shallow water type modelling approach in Tsunami-HySEA is considered adequate, as dispersive effects (e.g. Glimsdal et al., 2013) are very limited.

The equations of motion and rheological model implemented in BingCLAW are described comprehensively in Kim et al. (2019). A key parameter for determining the tsunamigenic potential is the initial yield strength, $\tau_{y,0}$, which we here set to 12kPa. Most important for determining the run-out distance and deposit thickness are the residual yield strength, $\tau_{y,\infty}$, and the remoulding parameter, Γ, set to 12kPa and 5×10^{-4} respectively. Kim et al. (2019) demonstrate how changes in each of these parameters affect both run-out areas and tsunami heights. Fig. 2 shows snapshots of the effective seafloor deformation from the BingCLAW landslide simulation at four instants ranging from 20 minutes after the slide initiation to over 4 hours later, at which point the most significant part of the slide mass is in its final position.

The landslide simulation was performed in geographical coordinates covering longitudes from 0 to 6.2 degrees East and latitudes from 62.60 to 66.06 degrees North with a lateral resolution of approximately 2 km. This spatial resolution was deemed adequate following extensive numerical convergence tests. The time-step for the landslide simulation is determined automatically according to a user-specified maximum CFL (Courant–Friedrichs–Lewy) number. Tsunami-HySEA interpolates the landslide deformation field provided by BingCLAW in the time domain, and a 60 second output interval from BingCLAW was deemed adequate for convergence. It can be shown that a coarser sampling interval than this, for this example, leads to an insufficiently smooth wave generation and wave generation that appears as a series of discontinuous waves.

Tsunami-HySEA interpolates the landslide input in time only and so the BingCLAW output needs to be interpolated onto a grid matching the nodes of the tsunami simulation exactly over the subset of the grid nodes covered by the landslide simulation. The tsunami simulation grid extended from 10.2 degrees West to 14.0 degrees East and from 49.6 to 68.2 degrees North. In order to demonstrate numerical convergence of the calculations, tsunami simulations were carried out at four different spatial resolutions: 0.02 degrees (2.2 km), 0.01 degrees (1.1 km), 0.005 degrees (556m), and 0.0025 (278m). Each refinement of spatial resolution is with a factor of 2, and hence a factor of 4 increase in the size of all files storing 2-dimensional variables. The netcdf file containing the seafloor deformation at the coarsest resolution is 85 MB; the equivalent file for the finest resolution is 5.4 GB. We note that the model of Clark et al. (2022b) is only provided at a resolution of 0.005° and so refinements beyond this cannot incorporate more information about the bathymetry itself. Also in Tsunami-HySEA, the time-step is not specified explicitly but calculated automatically within the program to satisfy the CFL condition.

2. Simulation Results

Fig. 3 shows maps of maximum sea surface elevation and time-series of surface elevation and velocities for simulations using both contemporary and palaeobathymetries. For most locations north west of Dogger Bank, the maximum sea surface elevation attained is marginally higher for the present-day bathymetry (panel a) than for the palaeobathymetry (panel b). The differences are however small and the results for the northern part of the North Sea are similar in the two images. Notable exceptions are, for example, along the northern coast of Doggerland where the presence of land in the palaeobathymetry leads to a slightly higher sea surface elevation than for the contemporary simulation, resulting from coastal reflections. In both models, the shallow waters to the north of Dogger Bank/Dogger Island result in lower maximum sea surface elevation than for the deeper waters on either side. The presence of the island and far shallower waters to the south east in the palaeobathymetry fundamentally alter the propagation. The water surface elevation is reduced greatly for the palaeobathymetry for all locations south east of Doggerland and the shallow water shelf that extends from the North Coast of Doggerland to the North of Denmark. Regions that would experience surface elevations exceeding a meter given present-day topography see wave amplitudes no greater than 30 cm for the palaeobathymetry.

Fig. 3c) displays time-series for both surface elevation and flow speed for both simulations for the point labelled N; in the present day North Sea, this location is in open water with approximately 50 m depth and, in the palaeobathymetries, it lies to the north of the coast of Dogger Island with approximately 20 m depth. The surface elevation at point N in the simulation with the present day bathymetry attains a maximum of over 2 m with several high peaks between 5 and 10 hours after the slide initiation, but a sharp decline in the wave heights after 10 hours. The onset of the first waves at point N for the palaeobathymetry is delayed by over an hour relative to that for the present-day bathymetry as a result of the shallower water. The maximum surface elevation attained exceeds 1 m for the palaeobathymetry; a little over half that obtained for the present-day bathymetry. The wave trains for the palaeobathymetry not only arrive later but persist at high amplitudes far longer, with the additive complication of coastal reflections from Doggerland. The maximum flow speed at point N in the present day bathymetry falls just short of 1 meter per second. For the palaeobathymetries, the current velocities exceed 1 m/s repeatedly over the course of many hours. For all simulations, the tsunami is largely diminished after 24 hours for point N.

Fig. 3d) displays the equivalent time-series for a location S, south of Dogger Bank/Doggerland, to the north of the coast of present-day Netherlands. The water depth at point S in the present-day bathymetry is around 40 m as opposed to around 10 m in the palaeobathymetric models. The first wave in the present-day simulation arrives around 8 hours after the slide, with surface elevations exceeding a meter in the hours that follow. The tsunami at the same location in the palaeobathymetric simulations do not arrive at point S until about 13 hours after the slide initiation; these waves are smaller by a factor of around 5 relative to the present-day simulation, and have far longer periods. At point S the flow speed reaches almost 0.5 m/s for the present-day simulation, almost a factor of 4 larger than for the palaeo-simulations. Although the locations N and S displayed are chosen relatively arbitrarily, the surface elevation and velocity time-series at these points are representative of the regions they are chosen from. Time-series from many more locations are available in the simulation output.

The differences in the tsunami travel-times between the simulations performed with present-day and palaeo-bathymetry are displayed in Fig. 4. It is stressed that these maps indicate the onset times of the initial wave; as we are reminded in Fig. 3, the highest surface elevations and velocities often occur several hours following the first wave arrival. North of Doggerland, the geometries of the isochrons are similar for the contemporary and palaeobathymetries. However, there is a clear retardation that is more pronounced to the east. The location of the northernmost tip of Doggerland lies close to the 5-hour isochron for the present-day simulation and close to the 6-hour isochron for the palaeobathymetry. It is to the south of Doggerland that the contrast in tsunami travel times between the present day and palaeo-models is greatest. The wave takes almost 15 hours to reach its most south-easterly point in the palaeo-simulation; this same location is reached after 9 hours in the present-day simulation.

Fig. 5 displays surface elevation as a function of time for both present-day and palaeo- tsunami simulations at a series of locations going from north to south offshore of what is estimated to be the past coastline of what is present-day Denmark (Clark et al., 2022b). At the northernmost location (Fig. 5a), at the edge of the Norwegian trench, there is little difference in the first arrival of the tsunami, either with respect to signal form, amplitude, and period, or with respect to arrival time. This is also expected given the similarity between the contemporary and palaeobathymetries both at that location and at intermediate locations between this location and the slide region. At the locations further south (Fig. 5 b,c,d,e), the wave onset for the palaeo-simulation is delayed progressively relative to the wave onset in the present-day simulation. The amplitudes and complexities of the tsunami in the palaeosimulations are diminished relative to their counterparts in the present-day simulations.

It remains to demonstrate that the decrease in maximum surface elevation and velocities in the southeastern North Sea indicated in our 0.02° resolution simulations are converged and are not significantly different if the simulations are performed at higher spatial and temporal resolution. The simulations at 0.02°, 0.01°, 0.005°, and 0.0025° resolutions completed within 5.34 minutes, 25 minutes, 3.04 hours, and 24.10 hours respectively, computed on a single NVIDIA Quadro GV100 GPU. The size of the files generated increase by a predictable factor of 4 for each halving of the length scale. The exact scaling factor for the increase in the time taken depends on multiple factors, both with regards to the properties of the tsunami itself and the computational hardware. The finest scale simulation takes 280 times longer to compute than the coarsest scale simulation and so determining adequate convergence at relatively coarse resolution is a sensible step before attempting large scale ensemble simulations.

Fig. 6 (panels a-d) displays the flow speed in the area of interest for the four different spatial resolutions for the palaeosimulations. The flow speed exceeds a meter per second north-west of Doggerland but diminishes to only a few centimeters per second in the most south-easterly part of the North Sea. A few smaller scale features appear in the higher resolution simulation that are not present at the coarsest resolution, although the overall picture is qualitatively identical. In particular, the flow speeds along the coastlines are not perceptibly different in the simulations at different spatial resolutions. Fig. 6 (panels e-f) displays the time-series for surface elevation, η, at locations marked N and S for all of the numerical resolutions tested. There are only relatively minor differences between the different curves and these are greatest long after the first wave arrival and, importantly, long after the maximum amplitudes are attained. The contributions to the time-series from waves reflected at the coastlines are greater at these later times and differences between the representations of the coastlines on the different resolution grids are the most likely sources of the discrepancies later in the simulations.

3. Sensitivity to bathymetry and location of coastline: a parametric study

Given the uncertainty regarding the water depth of the southern North Sea for 8150 cal BP, and the first order effect that this has on the extent and characteristics of the tsunami, it is necessary to address the sensitivity of tsunami metrics to the topobathymetry in a meaningful way. Covering all eventualities of palaeobathymetries, in which arbitrary variations in the depth profiles are permitted, is of course intractable. However, given any palaeobathymetric model and the present topobathymetry, we can define a continuum of models parametrized by a single parameter λ ranging from the palaeo-model for, say, $\lambda = 0$ and the present day model for $\lambda = 1$, with intermediate models varying linearly with λ for all locations, i.e.

$$d_{\lambda}(x, y) = d_{\text{palaeo}}(x, y).(1 - \lambda) + d_{\text{present}}(x, y).\lambda \quad (1)$$

defined for λ between zero and unity (here x denotes longitude and y denotes latitude). For a range of λ, we can repeat the entire workflow and calculate the degree to which the tsunami characteristics vary for the different bathymetric models. We have two points of departure for the functions $d_{\text{palaeo}}(x, y)$: the models of Clark et al. (2022b) and Hill et al. (2014).

Fig.7 displays for a range of different models of the the bathymetry and coastlines, the maximum water surface elevation, and the flow speed along a profile extending from a point X (55.50°N, 1.50°E), north of Dogger Bank, to a point G (54.33°N, 8.78°E) located at the present-day settlement of Garding. Fig.7 a) shows $d_{\lambda}(x, y)$ for 12 different models: 11 models linearly interpolated between the Clark et al. (2022b) palaeobathymetry ($\lambda = 0$) and the present-day bathymetry ($\lambda = 1$), and a single curve (red dashes) indicating $d_{\text{Hill et al.}}(x, y)$. Grey shapes mark the approximate extent of the region of Dogger Bank that is above sea level for the palaeo-models, as well as the approximate present-day extent of land near Garding. Only for the models with $\lambda = 0.0$ and $\lambda = 0.1$ is there land above sea level at Dogger Bank. For all other values, it is totally submerged beneath at least a few meters of water. The model of Hill et al. (2014) has the above sea-level part of Dogger Bank slightly to the north of the island defined by the Clark et al. (2022b) topobathymetry, which follows the general form of the present-day topobathymetry more closely than that of Hill et al. (2014). At the south-eastern end of the profile, the coast is reached about 120 km from point G for the model of Clark et al. (2022b) and about 100 km from point G for the model of Hill et al. (2014).

Fig.7c) displays the maximum sea surface elevation attained along the profile for each of the bathymetric models. Almost everywhere, the greatest values are obtained for the present day bathymetry; the only exceptions are in near-shore regions where the water surface elevation is more sensitive to the exact shape of the sea floor. Only for three of the curves is there a land gap in the Dogger Bank region but, for many more of the curves, there is a significant reduction in the maximum offshore water surface elevation attained. For these models, the depth of water close over Dogger Bank is less than 10 meters. This region of shallow water presents a significant barrier to tsunami propagation in the North Sea south east of Dogger Bank. For the smaller values of λ, for which the topobathymetry becomes closer and closer to the model of Clark et al. (2022b), we see two effects. First, the reach of the tsunami propagation stops further and further from point G, retreating with the coastline. Second, the maximum water surface elevation diminishes over the entire profile as the water depth is reduced.

Fig.7d) displays the flow speed along the same profile. At the eastern end of the profile the highest velocities are for the present day bathymetry, reaching approximately 1 m/s. North of Dogger Bank, the situation is reversed with the greatest velocities attained for the profiles closest to the Clark et al. (2022b) bathymetry. The curve for the Hill et al. (2014) indicates far greater velocities close to the coast of Doggerland. However, we advise against drawing too strong conclusions from the maximum flow speed profile as it is likely sensitive to variations in the depth at lateral scales that may not be very well resolved. This can be concluded from the contrast between the curves for the Hill et al. (2014) and Clark et al. (2022b) models. The curves for maximum water surface elevation (Fig.7c) vary far more smoothly with depth along the profile.

Fig. 8 is entirely analogous to Fig. 7 except for that it covers a different profile extending from a point Y (56.90°N, 4.40°E) to the same point G at Garding. A crucial difference between the profiles X-G and Y-G is that the profile in Fig. 8 has no land barrier between the open sea and the coastline. The general properties of the tsunami metrics are analogous in the two profiles; both the maximum surface elevation and the maximum velocity decreases as we move further from the present day topobathymetry and closer to the palaeobathymetric models. The profile crosses the fully submerged Dogger Bank at approximately 100 km from point Y. For the profiles closest to the present day bathymetry, the maximum surface elevation either remains largely unchanged or decreases gradually. For the profiles closest to the Clark et al. (2022b) palaeobathymetry, there is a rapid decrease in the maximum surface elevation beyond 100 km from point Y. Although the maximum surface elevation curves vary quite smoothly with λ, a depth of around 30 m at Dogger Bank appears to mark a boundary between the profiles for which the decrease is abrupt and the profiles for which the decrease is gradual.

4. Conclusions and discussion

We have demonstrated using numerical simulations of the Storegga slide and tsunami that the presence of Dogger Bank and the significantly shallower waters of the North Sea to the south presented a significant impediment to the tsunami wave propagation. Based on the input from the palaeobathymetric reconstructions from Hill et al. (2014) and Clark et al. (2022b) combined with numerical modelling results, the tsunami surface elevation is not likely to have exceeded a meter to the south-east of Dogger Bank. Similarly, the maximum velocities and maximum momentum flux calculated in this region using the same palaeobathymetric reconstructions as input are significantly lower than those predicted using present day bathymetry. These simulation results support previous results (c.f. Walker et al., 2020) that the impact of the tsunami on the Dogger Island itself, if still present at the time of Storegga, would not have been catastrophic.

However, research based on field investigations have recently claimed that Storegga tsunami deposits occur as far south as the SW coast of Denmark and at the German North Sea coast. From one sediment core at Rømø, Denmark (Fruergaard et al., 2015b) and two at the same location at Garding, Germany, Garding-2A (Vött et al., 2024) and Garding-2 (Zhang et al., 2014) (Fig. 1), radiocarbon dates and optical stimulated luminescence (OSL) dates document that about 2000 and 5000 years of sedimentation is missing at Rømø and Garding respectively. The subsequent layer deposited on top of this erosive surface has shell-rich sand layers and rip-up clasts, like other tsunami deposits. Based on this, Fruergaard et al. (2015b) and Vött et al. (2024) claim that the Storegga tsunami inundated the estuaries tens of kilometers inland in northern Germany and a sediment run-up of 1.5–5.5 meters at Rømø in Denmark. Based on the tsunami modelling results using the palaeobathymetric reconstructions as input, this mechanism is not possible. In order to provide tsunami current velocities capable of causing the deposits we show through the sensitivity studies that the bathymetry, from the location of the slide to the coast of interest, would have to have been similar to the present day situation, which we find unlikely.

An alternative interpretation to the sites at Rømø and Garding is that the erosion and deposition is caused by the Holocene sea level rise (Fig. 9). Between 8 and 7 ka, the sea flooded the region forming a distinctive erosive surface (Fruergaard et al., 2015a) called a wave ravinement surface (Zecchin et al., 2019). Such a surface may be covered by a deposit reworked from the underlying substrate that could share many of the characteristics of true tsunami deposits. We think that it might be possible that this deposit, that was inferred to be a Storegga tsunami deposit at Rømø and Garding (Fruergaard et al., 2015b), instead is a lag deposit caused by sea level rise and related erosion during the transgression.

Zhang et al. (2014) interpreted this hiatus and shell-rich layer as we suggest above: as the beginning of the Holocene transgression. They wrote: "Generally, fragments of limnic muds and peat as well as a shell-rich layer are found at the base of the Holocene sequences in the North Sea area, which have been considered to be the beginning of the Holocene transgression. . . .. It is widely known that the Holocene transgression was accompanied by an erosion of the pre-existing surface deposits." The lowest radiocarbon dated shell to the erosive surface at Garding (Zhang et al., 2014) was dated to 7750 ± 320 cal yr BP (2σ-range), calibrated with Marine20 (Heaton et al., 2020) and $\Delta R = -19 \pm 140$ (Vött et al., 2024) and is a strong indication that the deposits in Garding are younger than the Storegga event, dated to 8140 ± 55 cal yr BP (2σ-range, Bondevik et al., 2024).

However, the radiocarbon and OSL ages from the R6 core at Rømø date the actual deposits to the time window of the Storegga tsunami. As pointed out by Fruergaard et al. (2015a), the gyttja overlying the "tsunami" sand layer contains remains of freshwater algae, is finely laminated, and interpreted by them to be in-situ. If our alternative interpretation is correct (Fig. 9), this gyttja containing freshwater algae must also be redeposited. We think it is possible that this segment of gyttja in the core could be a large piece ripped up from the gyttja below the hiatus (Fruergaard et al., 2015a). Our alternative interpretation should be tested by a re-investigation of the R6 core and/or new cores from the same site.

In presenting a continuum of candidate land-sea floor depth models from the present-day bathymetry to each of two alternative palaeobathymetries, we hope to have covered the range of plausible candidates for the true topobathymetry 8150 years ago. We note that a shallow Dogger Bank and shelf present a significant barrier to tsunami propagation even for many of the models for which no land is above sea level. For almost all of the models, the line extending along the northern coast of Doggerland and towards the northern tip of Denmark represents a boundary south of which the tsunami surface elevation and velocities are greatly diminished. Therefore, not even the presence of locally deeper features such as the Elbe Palaeovalley (e.g. Özmaral et al., 2022), not represented in either of the palaeobathymetric models used, would result in tsunami waves comparable with those that would be propagated under the present day bathymetry. To get a significant tsunami wave height and velocity near to Rømø or Garding, we would need a seafloor profile qualitatively different to that from the palaeobathymetric reconstructions from Hill et al. (2014) and Clark et al. (2022b) extending far out into the North Sea.

Along the Scottish coast, the nearest coast of comparable setting and geology to the Danish coast, where the Storegga run-up is securely reconstructed to 3–6 m (Smith, 2004), there is very little evidence of erosion. The lower boundary is usually sharp but show little variation that could be attributed to erosion. In most places radiocarbon dates below the lower boundary gives Storegga age. Scotland is much closer to Storegga, and the run-up reconstructions agree with the numerical modelling presented. Wave and depth conditions needed offshore Denmark to achieve the observed amounts of erosion from a tsunami approaching such a wide coast must be then much higher than reconstructed for the Scottish coast. This appears unlikely, even from the simulations given the present day bathymetry.

Uncertainty in the former topography around Dogger Bank is relatively large. The central portion of Dogger Bank, addressed by Emery et al. (2019, 2020) was likely to have already been submerged by the time of Storegga (Emery, 2020). The uncertainty in the timing and extent of the Eurasian Ice Sheet complex over Dogger Bank as used in GIA models (Clark et al., 2022b; Bradley et al., 2023) also leads to uncertainty in RSL changes after the LGM, which also affects the palaeobathymetry used in the models. RSL in the Dogger Bank region was potentially up to 10 m higher than that modelled by Clark et al. (2022b), although still within the continuum range presented here, and still resulting in a large barrier to tsunami propagation across the southeastern North Sea.

The uncertainties associated with the maximum flow depth on land and the inundation distances have contributions from every model assumption in the chain. Uncertainties regarding the slide volume and dynamics will propagate into the wave generation. The offshore wave propagation will depend fundamentally on the accuracy of the bathymetric model and on the numerical representation of the tsunami propagation. We have tried to address the uncertainty in the topobathymetry by providing a continuum of models between existing palaeobathymetric models and the present-day topobathymetry. The tsunami impact from Storegga in this region is greater given the present day bathymetry than in any of the probable palaeobathymetries and, even with today's seafloor, the impact in this region of the North Sea would be highly limited. Although the aforementioned uncertainties remain, we consider our simulation the most accurate to date especially due to the availability of the palaeobathymetric dataset by Clark et al. (2022b) which validated the GIA model against available chronological and geomorphological evidence of ice extent, biased to the abundance of data from the present-day coastline (Bradley et al., 2023). With regards to model details, our making available of all simulation output will hopefully provide a basis for quantitative comparison for subsequent studies.

Acknowledgements

We appreciate greatly comments and questions from Mikkel Fruergaard which have improved this manuscript significantly.

Data availability

The contemporary bathymetry model was obtained from
`https://www.gebco.net/data-products/gridded-bathymetry-data`
(GEBCO Bathymetric Compilation Group, 2024).

The palaeo-bathymetry relating to the study of Clark et al. (2022b) was obtained from
`https://doi.org/10.1594/PANGAEA.945729`
(Clark et al., 2022a).

The palaeo-bathymetry relating to the study of Hill et al. (2014) was provided to us by Jon Hill (pers. comm.). A copy of it can be obtained in the file `Hill_GEBCO_lambda_0.000.grd` available from `https://doi.org/10.82554/sdl-121`.

The BingCLAW code, including the Storegga landslide simulation example, is available from
`https://github.com/norwegian-geotechnical-institute/BingCLAW_5.6.1`
and described by Kim et al. (2019). The code and examples are permanently archived under Zenodo with the DOI
`https://doi.org/10.5281/zenodo.7695421`.

The Tsunami-HySEA code is administered by the EDANYA group at the University of Málaga with contact details at
`https://edanya.uma.es/hysea/index.php/models/tsunami-hysea`

The interface module that provided compatibility between the output from BingCLAW and the Tsunami-HySEA program is found on
https://github.com/dtgeoeu-wp6-tsunamis/Interface-module

The GMT software Wessel et al. (2019) was used to generate the maps displayed in this paper.

All numerical simulation outputs are openly available for download from the Geo-INQUIRE Simulation Data Lake, hosted by CINECA. The landslide simulation and the numerical convergence tests are found on
https://doi.org/10.82554/sdl-56.31 and the simulations for the topobathymetries in the parametrizations between the present day topobathymetry and the palaeobathymetries are found under
https://doi.org/10.82554/sdl-121.

Statement on the Use of AI Tools

No Artificial Intelligence tools were used in the writing of this manuscript. Microsoft Copilot was used to write simple python tools for coordinate transformations and spatial interpolation of netcdf files.

Funding

Preparation of the code used to simulate the Storegga landslide was partly performed under the Geo-INQUIRE project, funded by the European Commission under project number 101058518 within the HORIZON-INFRA-2021-SERV-01 call. The tsunami simulations and development of the Interface Module were supported by the EU project "A Digital Twin for Geophysical Extremes" (DT-GEO) and received funding from Horizon Europe under Grant Agreement No 101058129. The Simulation Data Lake (SDL) hosting the numerical simulation results is also funded by Geo-INQUIRE. Some development of the Tsunami-HySEA code was undertaken within the Center of Excellence of Exascale in Solid Earth (ChEESE) and under project PCI2022-134989-2 funded by
MCIN/AEI/10.13039/501100011033 and by the European Union NextGenerationEU/PRTR. ChEESE is funded by the European Union and has received funding from the European High Performance Computing Joint Undertaking (JU) and Spain, Italy, Iceland, Germany, Norway, France, Finland and Croatia under grant agreement No 101093038, ChEESE-2P. NGI received co-funding from the Research Council of Norway under project number 342515 for its participation in the ChEESE-2P project.

CRediT authorship contribution statement

Steven J. Gibbons: Conceptualization of study, execution of numerical models, interpretation of results, visualization, preparation of manuscript. **Stein Bondevik:** Interpretation of results and deposits, preparation of manuscript. **Bartosz Kurjanski:** Preparation of numerical model, interpretation of results, preparation of manuscript. **Marc**

de la Asunción: Programming of numerical model, interpretation of results, preparation of manuscript. **Valentina Magni:** Programming numerical model, interpretation of results, preparation of manuscript. **Jorge Macías Sánchez:** Programming of numerical model, interpretation of results, preparation of manuscript. **Andy R. Emery:** Interpretation of results, preparation of manuscript. **Finn Løvholt:** Experiment design, interpretation of results, preparation of manuscript.

References

de la Asunción, M., Castro, M.J., Fernández-Nieto, E., Mantas, J.M., Acosta, S.O., González-Vida, J.M., 2013. Efficient GPU implementation of a two waves TVD-WAF method for the two-dimensional one layer shallow water system on structured meshes. Computers & Fluids 80, 441–452. doi:10.1016/j.compfluid.2012.01.012. publisher: Pergamon.

Berger, M.J., George, D.L., LeVeque, R.J., Mandli, K.T., 2011. The GeoClaw software for depth-averaged flows with adaptive refinement. Advances in Water Resources 34, 1195–1206. doi:10.1016/j.advwatres.2011.02.016.

Bondevik, S., 2019. Tsunami from the Storegga Landslide, in: Meyers, R.A. (Ed.), Encyclopedia of Complexity and Systems Science. Springer Berlin Heidelberg, Berlin, Heidelberg, pp. 1–33. doi:10.1007/978-3-642-27737-5_644-1.

Bondevik, S., Løvholt, F., Harbitz, C., Mangerud, J., Dawson, A., Inge Svendsen, J., 2005. The Storegga Slide tsunami — comparing field observations with numerical simulations. Marine and Petroleum Geology 22, 195–208. doi:10.1016/j.marpetgeo.2004.10.003.

Bondevik, S., Mangerud, J., Dawson, S., Dawson, A., Lohne, Ö., 2003. Record-breaking height for 8000-year-old tsunami in the North Atlantic. Eos, Transactions American Geophysical Union 84, 289–293. doi:10.1029/2003EO310001.

Bondevik, S., Risebrobakken, B., Gibbons, S.J., Rasmussen, T.L., Løvholt, F., 2024. Contamination of 8.2 ka cold climate records by the Storegga tsunami in the Nordic Seas. Nature Communications 15, 2904. doi:10.1038/s41467-024-47347-9.

Bondevik, S., Svendsen, J.I., Johnsen, G., Mangerud, J., Kaland, P.E., 1997a. The Storegga tsunami along the Norwegian coast, its age and run up. Boreas 26, 29–53. doi:10.1111/j.1502-3885.1997.tb00649.x.

Bondevik, S., Svendsen, J.I., Mangerud, J., 1997b. Tsunami sedimentary facies deposited by the Storegga tsunami in shallow marine basins and coastal lakes, western Norway. Sedimentology 44, 1115–1131. doi:10.1046/j.1365-3091.1997.d01-63.x.

Bradley, S.L., Ely, J.C., Clark, C.D., Edwards, R.J., Shennan, I., 2023. Reconstruction of the palaeo-sea level of Britain and Ireland arising from empirical constraints of ice extent: implications for regional sea level forecasts and North American ice sheet volume. Journal of Quaternary Science 38, 791–805. doi:10.1002/jqs.3523.

Bradley, S.L., Milne, G.A., Shennan, I., Edwards, R., 2011. An improved glacial isostatic adjustment model for the British Isles. Journal of Quaternary Science 26, 541–552. doi:10.1002/jqs.1481.

Bryn, P., Berg, K., Forsberg, C.F., Solheim, A., Kvalstad, T.J., 2005. Explaining the Storegga Slide. Marine and Petroleum Geology 22, 11–19. doi:10.1016/j.marpetgeo.2004.12.003.

Bugge, T., Belderson, R.H., Kenyon, N.H., 1988. The Storegga Slide. Philosophical Transactions of the Royal Society A: Mathematical, Physical and Engineering Sciences 325, 357–388. doi:10.1098/rsta.1988.0055.

Clark, C.D., Ely, J.C., Fabel, D., Bradley, S.L., 2022a. BRITICE-CHRONO maps and GIS data of the last British-Irish Ice Sheet 31 to 15 ka, including model reconstruction, geochronometric age spreadsheet, palaeotopographies and coastline positions. URL: https://doi.org/10.1594/PANGAEA.945729, doi:10.1594/PANGAEA.945729.

Clark, C.D., Ely, J.C., Hindmarsh, R.C.A., Bradley, S., Ignéczi, A., Fabel, D., Ó Cofaigh, C., Chiverrell, R.C., Scourse, J., Benetti, S., Bradwell, T., Evans, D.J.A., Roberts, D.H., Burke, M., Callard, S.L., Medialdea, A., Saher, M., Small, D., Smedley, R.K., Gasson, E., Gregoire, L., Gandy, N., Hughes, A.L.C., Ballantyne, C., Bateman, M.D., Bigg, G.R., Doole, J., Dove, D., Duller, G.A.T., Jenkins, G.T.H., Livingstone, S.L., McCarron, S., Moreton, S., Pollard, D., Praeg, D., Sejrup, H.P., Van Landeghem, K.J.J., Wilson, P., 2022b. Growth and retreat of the last British–Irish Ice Sheet, 31 000 to 15 000 years ago: the BRITICE-CHRONO reconstruction. Boreas 51, 699–758. doi:10.1111/bor.12594.

Clark, C.D., Hughes, A.L., Greenwood, S.L., Jordan, C., Sejrup, H.P., 2012. Pattern and timing of retreat of the last British-Irish Ice Sheet. Quaternary Science Reviews 44, 112–146. doi:10.1016/j.quascirev.2010.07.019.

Devendra, D., Łacka, M., Szymańska, N., Nethupul, H., Pawłowska, J., Szymczak-Żyła, M., Krajewska, M., Silva, P.D., Bondevik, S., Gibbons, S.J., Zajaczkowski, M., 2025. Expanding the footprint of the storegga tsunami through new evidence from arctic marine sediments. Scientific Reports 15, 24809. doi:10.1038/s41598-025-10811-7.

Earland, J.L., Scourse, J.D., Ehmen, T., Kender, S., Ascough, P., 2024. Identification of the Storegga event offshore Shetland. Marine Geology 474, 107334. doi:10.1016/j.margeo.2024.107334.

Emery, A.R., 2020. Glacial and postglacial landscape evolution at dogger bank since the last glacial maximum. phd. University of Leeds. URL: https://etheses.whiterose.ac.uk/id/eprint/27519/.

Emery, A.R., Hodgson, D.M., Barlow, N.L., Carrivick, J.L., Cotterill, C.J., Mellett, C.L., Booth, A.D., 2019. Topographic and hydrodynamic controls on barrier retreat and preservation: An example from Dogger Bank, North Sea. Marine Geology 416, 105981. doi:10.1016/j.margeo.2019.105981.

Emery, A.R., Hodgson, D.M., Barlow, N.L.M., Carrivick, J.L., Cotterill, C.J., Richardson, J.C., Ivanovic, R.F., Mellett, C.L., 2020. Ice sheet and palaeoclimate controls on drainage network evolution: an example from Dogger Bank, North Sea. Earth Surface Dynamics 8, 869–891. doi:10.5194/esurf-8-869-2020.

Folch, A., Abril, C., Afanasiev, M., Amati, G., Bader, M., Badia, R.M., Bayraktar, H.B., Barsotti, S., Basili, R., Bernardi, F., Boehm, C., Brizuela, B., Brogi, F., Cabrera, E., Casarotti, E., Castro, M.J., Cerminara, M., Cirella, A., Cheptsov, A., Conejero, J., Costa, A., de la Asunción, M., de la Puente, J., Djuric, M., Dorozhinskii, R., Espinosa, G., Esposti-Ongaro, T., Farnós, J., Favretto-Cristini, N., Fichtner, A., Fournier, A., Gabriel, A.A., Gallard, J.M., Gibbons, S.J., Glimsdal, S., González-Vida, J.M., Gracia, J., Gregorio, R., Gutierrez, N., Halldorsson, B., Hamitou, O., Houzeaux, G., Jaure, S., Kessar, M., Krenz, L., Krischer, L., Laforet, S., Lanucara, P., Li, B., Lorenzino, M.C., Lorito, S., Løvholt, F., Macedonio, G., Macías, J., Marín, G., Martínez Montesinos, B., Mingari, L., Moguilny, G., Montellier, V., Monterrubio-Velasco, M., Moulard, G.E., Nagaso, M., Nazaria, M., Niethammer, C., Pardini, F., Pienkowska, M., Pizzimenti, L., Poiata, N., Rannabauer, L., Rojas, O., Rodriguez, J.E., Romano, F., Rudyy, O., Ruggiero, V., Samfass, P., Sánchez-Linares, C., Sanchez, S., Sandri, L., Scala, A., Schaeffer, N., Schuchart, J., Selva, J., Sergeant, A., Stallone, A., Taroni, M., Thrastarson, S., Titos, M., Tonelllo, N., Tonini, R., Ulrich, T., Vilotte, J.P., Vöge, M., Volpe, M., Aniko Wirp, S., Wössner, U., 2023. The EU Center of Excellence for Exascale in Solid Earth (ChEESE): Implementation, results, and roadmap for the second phase. Future Generation Computer Systems , S0167739X23001401doi:10.1016/j.future.2023.04.006.

Fruergaard, M., Andersen, T.J., Nielsen, L.H., Johannessen, P.N., Aagaard, T., Pejrup, M., 2015a. High-resolution reconstruction of a coastal barrier system: impact of Holocene sea-level change. Sedimentology 62, 928–969. doi:10.1111/sed.12167.

Fruergaard, M., Piasecki, S., Johannessen, P., Noe-Nygaard, N., Andersen, T., Pejrup, M., Nielsen, L., 2015b. Tsunami propagation over a wide, shallow continental shelf caused by the Storegga slide, southeastern North Sea, Denmark. Geology , G37151.1doi:10.1130/G37151.1.

Gauer, P., Kvalstad, T.J., Forsberg, C.F., Bryn, P., Berg, K., 2005. The last phase of the Storegga Slide: simulation of retrogressive slide dynamics and comparison with slide-scar morphology. Marine and Petroleum Geology 22, 171–178. doi:10.1016/j.marpetgeo.2004.10.004.

GEBCO Bathymetric Compilation Group, 2024. The GEBCO_2024 Grid - a continuous terrain model of the global oceans and land. URL: https://www.bodc.ac.uk/data/published_data_library/catalogue/10.5285/1c44ce99-0a0d-5f4f-e063-7086abc0ea0f/, doi:10.5285/1C44CE99-0A0D-5F4F-E063-7086ABC0EA0F.

Glimsdal, S., Pedersen, G.K., Harbitz, C.B., Løvholt, F., 2013. Dispersion of tsunamis: does it really matter? Natural Hazards and Earth System Sciences 13, 1507–1526. doi:10.5194/nhess-13-1507-2013.

Haflidason, H., Lien, R., Sejrup, H.P., Forsberg, C.F., Bryn, P., 2005. The dating and morphometry of the Storegga Slide. Marine and Petroleum Geology 22, 123–136. doi:10.1016/j.marpetgeo.2004.10.008.

Haflidason, H., Sejrup, H.P., Nygård, A., Mienert, J., Bryn, P., Lien, R., Forsberg, C.F., Berg, K., Masson, D., 2004. The Storegga Slide: architecture, geometry and slide development. Marine Geology 213, 201–234. doi:10.1016/j.margeo.2004.10.007.

Harbitz, C., 1992. Model simulations of tsunamis generated by the Storegga Slides. Marine Geology 105, 1–21. doi:10.1016/0025-3227(92)90178-k.

Harbitz, C.B., Løvholt, F., Pedersen, G., Masson, D.G., 2006. Mechanisms of tsunami generation by submarine landslides: A short review. Norsk Geologisk Tidsskrift 86, 255–264.

Heaton, T.J., Köhler, P., Butzin, M., Bard, E., Reimer, R.W., Austin, W.E.N., Bronk Ramsey, C., Grootes, P.M., Hughen, K.A., Kromer, B., Reimer, P.J., Adkins, J., Burke, A., Cook, M.S., Olsen, J., Skinner, L.C., 2020. Marine20—The Marine Radiocarbon Age Calibration Curve (0–55,000 cal BP). Radiocarbon 62, 779–820. URL: https://www.cambridge.org/core/product/identifier/S0033822220000685/type/journal_article, doi:10.1017/RDC.2020.68.

Hill, J., Collins, G.S., Avdis, A., Kramer, S.C., Piggott, M.D., 2014. How does multiscale modelling and inclusion of realistic palaeobathymetry affect numerical simulation of the Storegga Slide tsunami? Ocean Modelling 83, 11–25. doi:10.1016/j.ocemod.2014.08.007.

Houmark-Nielsen, M., 2004. The Pleistocene of Denmark: a review of stratigraphy and glaciation history, in: Gibbard, P.L., Ehlers, J. (Eds.), Developments in Quaternary Sciences. Elsevier. volume 2, pp. 35–46. doi:10.1016/S1571-0866(04)80055-1.

Karstens, J., Haflidason, H., Berndt, C., Crutchley, G.J., 2023. Revised Storegga Slide reconstruction reveals two major submarine landslides 12,000 years apart. Communications Earth & Environment 4, 55. doi:10.1038/s43247-023-00710-y.

Kim, J., Løvholt, F., Issler, D., Forsberg, C.F., 2019. Landslide Material Control on Tsunami Genesis: The Storegga Slide and Tsunami (8,100 Years BP). Journal of Geophysical Research: Oceans 124, 3607–3627. doi:10.1029/2018JC014893.

Kvalstad, T.J., Andresen, L., Forsberg, C.F., Berg, K., Bryn, P., Wangen, M., 2005. The Storegga slide: evaluation of triggering sources and slide mechanics. Marine and Petroleum Geology 22, 245–256. doi:10.1016/j.marpetgeo.2004.10.019.

Lambeck, K., Smither, C., Johnston, P., 1998. Sea-level change, glacial rebound and mantle viscosity fornorthern Europe. Geophysical Journal International 134, 102–144. doi:10.1046/j.1365-246x.1998.00541.x.

Leveque, R.J., George, D.L., Berger, M.J., 2011. Tsunami modelling with adaptively refined finite volume methods. Acta Numerica 20, 211–289. doi:10.1017/S0962492911000043.

Liu, Z., L'Heureux, J.S., Glimsdal, S., Lacasse, S., 2021. Modelling of mobility of rissa landslide and following tsunami. Computers and Geotechnics 140, 104388. doi:https://doi.org/10.1016/j.compgeo.2021.104388.

Løvholt, F., Pedersen, G., Harbitz, C.B., Glimsdal, S., Kim, J., 2015. On the characteristics of landslide tsunamis. Philosophical Transactions of the Royal Society A: Mathematical, Physical and Engineering Sciences 373, 20140376. doi:10.1098/rsta.2014.0376.

Løvholt, F., Schulten, I., Mosher, D., Harbitz, C., Krastel, S., 2019. Modelling the 1929 grand banks slump and landslide tsunami. Geological Society, London, Special Publications 477, 315–331. doi:10.1144/SP477.28.

Løvholt, F., Bondevik, S., Laberg, J.S., Kim, J., Boylan, N., 2017. Some giant submarine landslides do not produce large tsunamis. Geophysical Research Letters 44, 8463–8472. doi:10.1002/2017GL074062.

Løvholt, F., Harbitz, C.B., Haugen, K.B., 2005. A parametric study of tsunamis generated by submarine slides in the Ormen Lange/Storegga area off western Norway. Marine and Petroleum Geology 22, 219–231. doi:10.1016/j.marpetgeo.2004.10.017.

Løvholt, F., Pedersen, G., Gisler, G., 2008. Oceanic propagation of a potential tsunami from the la palma island. Journal of Geophysical Research: Oceans 113. URL: https://agupubs.onlinelibrary.wiley.com/doi/abs/10.1029/2007JC004603, doi:https://doi.org/10.1029/2007JC004603, arXiv:https://agupubs.onlinelibrary.wiley.com/doi/pdf/10.1029/2007JC004603.

Løvholt, F., Pedersen, G., Glimsdal, S., 2010. Coupling of Dispersive Tsunami Propagation and Shallow Water Coastal Response. The Open Oceanography Journal 4, 71–82. doi:10.2174/1874252101004010071.

Macías, J., Castro, M.J., Escalante, C., 2020a. Performance assessment of the Tsunami-HySEA model for NTHMP tsunami currents benchmarking. Laboratory data. Coastal Engineering 158, 103667. doi:10.1016/j.coastaleng.2020.103667.

Macías, J., Castro, M.J., Escalante, C., 2020b. Performance assessment of the Tsunami-HySEA model for NTHMP tsunami currents benchmarking. Laboratory data. Coastal Engineering 158, 103667. doi:10.1016/j.coastaleng.2020.103667.

Macías, J., Castro, M.J., Ortega, S., Escalante, C., González-Vida, J.M., 2017. Performance Benchmarking of Tsunami-HySEA Model for NTHMP's Inundation Mapping Activities. Pure and Applied Geophysics 174, 3147–3183. doi:10.1007/s00024-017-1583-1.

Macías, J., Escalante, C., Castro, M.J., 2021. Multilayer-HySEA model validation for landslide-generated tsunamis – Part 2: Granular slides. Natural Hazards and Earth System Sciences 21, 791–805. doi:10.5194/nhess-21-791-2021.

Özmaral, A., Abegunrin, A., Keil, H., Hepp, D.A., Schwenk, T., Lantzsch, H., Mörz, T., Spiess, V., 2022. The Elbe Palaeovalley: Evolution from an ice-marginal valley to a sedimentary trap (SE North Sea). Quaternary Science Reviews 282, 107453. doi:10.1016/j.quascirev.2022.107453.

Patton, H., Hubbard, A., Andreassen, K., Auriac, A., Whitehouse, P.L., Stroeven, A.P., Shackleton, C., Winsborrow, M., Heyman, J., Hall, A.M., 2017. Deglaciation of the Eurasian ice sheet complex. Quaternary Science Reviews 169, 148–172. doi:10.1016/j.quascirev.2017.05.019.

Reimer, P.J., Austin, W.E.N., Bard, E., Bayliss, A., Blackwell, P.G., Bronk Ramsey, C., Butzin, M., Cheng, H., Edwards, R.L., Friedrich, M., Grootes, P.M., Guilderson, T.P., Hajdas, I., Heaton, T.J., Hogg, A.G., Hughen, K.A., Kromer, B., Manning, S.W., Muscheler, R., Palmer, J.G., Pearson, C., Van Der Plicht, J., Reimer, R.W., Richards, D.A., Scott, E.M., Southon, J.R., Turney, C.S.M., Wacker, L., Adolphi, F., Büntgen, U., Capano, M., Fahrni, S.M., Fogtmann-Schulz, A., Friedrich, R., Köhler, P., Kudsk, S., Miyake, F., Olsen, J., Reinig, F., Sakamoto, M., Sookdeo, A., Talamo, S., 2020. The IntCal20 Northern Hemisphere Radiocarbon Age Calibration Curve (0–55 cal kBP). Radiocarbon 62, 725–757. doi:10.1017/RDC.2020.41.

Rydgren, K., Bondevik, S., 2015. Moss growth patterns and timing of human exposure to a Mesolithic tsunami in the North Atlantic. Geology 43, 111–114. doi:10.1130/G36278.1.

Shennan, I., Bradley, S.L., Edwards, R., 2018. Relative sea-level changes and crustal movements in Britain and Ireland since the Last Glacial Maximum. Quaternary Science Reviews 188, 143–159. doi:10.1016/j.quascirev.2018.03.031.

Smith, D., 2004. The Holocene Storegga Slide tsunami in the United Kingdom. Quaternary Science Reviews 23, 2291–2321. doi:10.1016/j.quascirev.2004.04.001.

Vanneste, M., Løvholt, F., Issler, D., Liu, Z., Boylan, N., Kim, J., 2019. A novel quasi-3d landslide dynamics model: From theory to applications and risk assessment, in: Proceedings of the Offshore Technology Conference, Houston, Texas, May 2019, p. D011S006R006. doi:10.4043/29363-MS.

Vött, A., Hadler, H., Willershäuser, T., Slabon, A., Slabon, L., Wahlen, H., Fischer, P., Bungenstock, F., Röbke, B.R., Frechen, M., Grube, A., Sirocko, F., 2024. Possible Indication of the Impact of the Storegga Slide Tsunami on the German North Sea Coast around 8150 cal BP. Geosciences 14, 262. doi:10.3390/geosciences14100262.

Walker, J., Gaffney, V., Fitch, S., Muru, M., Fraser, A., Bates, M., Bates, R., 2020. A great wave: the Storegga tsunami and the end of Doggerland? Antiquity 94, 1409–1425. doi:10.15184/aqy.2020.49.

Walker, J., Nyland, A.J., Bergsvik, K.A., Kilhavn, H., Gibbons, S.J., Glimsdal, S., 2024. A multiproxy approach to understanding the impact of the Storegga tsunami upon Mesolithic hunter-fisher-gatherers across different regions of western Norway. Quaternary Science Reviews 324, 108433. doi:10.1016/j.quascirev.2023.108433.

Wessel, P., Luis, J.F., Uieda, L., Scharroo, R., Wobbe, F., Smith, W.H.F., Tian, D., 2019. The Generic Mapping Tools Version 6. Geochemistry, Geophysics, Geosystems 20, 5556–5564. doi:10.1029/2019GC008515.

Zecchin, M., Catuneanu, O., Caffau, M., 2019. Wave-ravinement surfaces: Classification and key characteristics. Earth-Science Reviews 188, 210–239. doi:10.1016/j.earscirev.2018.11.011.

Zengaffinen-Morris, T., Urgeles, R., Løvholt, F., 2022. On the inference of tsunami uncertainties from landslide run-out observations. Journal of Geophysical Research: Oceans 127, e2021JC018033. doi:https://doi.org/10.1029/2021JC018033. e2021JC018033 2021JC018033.

Zhang, J., Tsukamoto, S., Grube, A., Frechen, M., 2014. OSL and 14C chronologies of a Holocene sedimentary record (Garding-2 core) from the German North Sea coast. Boreas 43, 856–868. doi:10.1111/bor.12071.

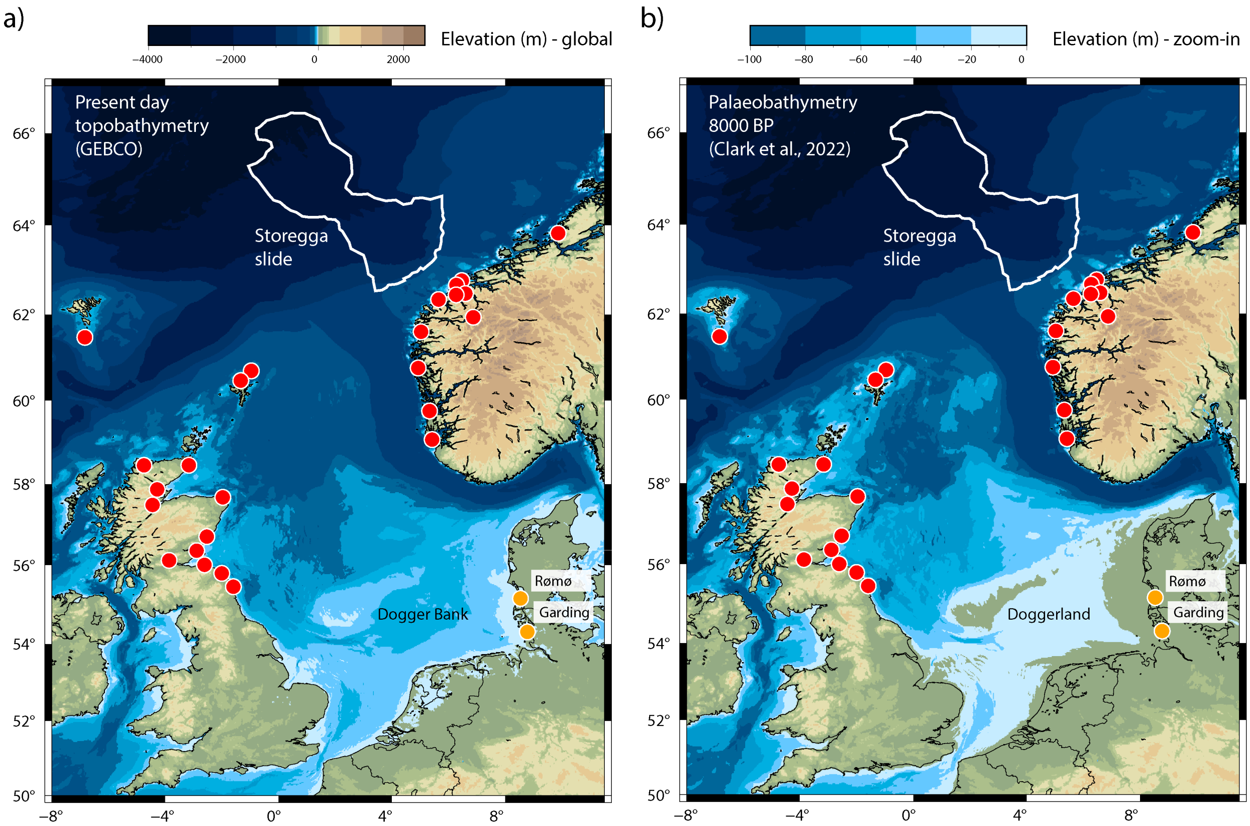

Figure 1: Bathymetry of the North Sea and surrounding regions, (a) for the present day (GEBCO Bathymetric Compilation Group, 2024) and (b) modelled for 8000 years Before Present (Clark et al., 2022b; Bradley et al., 2023). The thick white line displays the outer boundary of the debris flow sediments from the Storegga slide as indicated by Haflidason et al. (2005). The red symbols mark the locations of Storegga deposits as given by Bondevik (2019). The orange circles mark Rømø, Denmark (8.533°E,55.157°N: Fruergaard et al., 2015b) and Garding, Germany (8.776°E, 54.304°N: Vött et al., 2024). A single colour palette is used to represent elevation, but the interval between sea level and 100m depth is also shown separately for clarity.

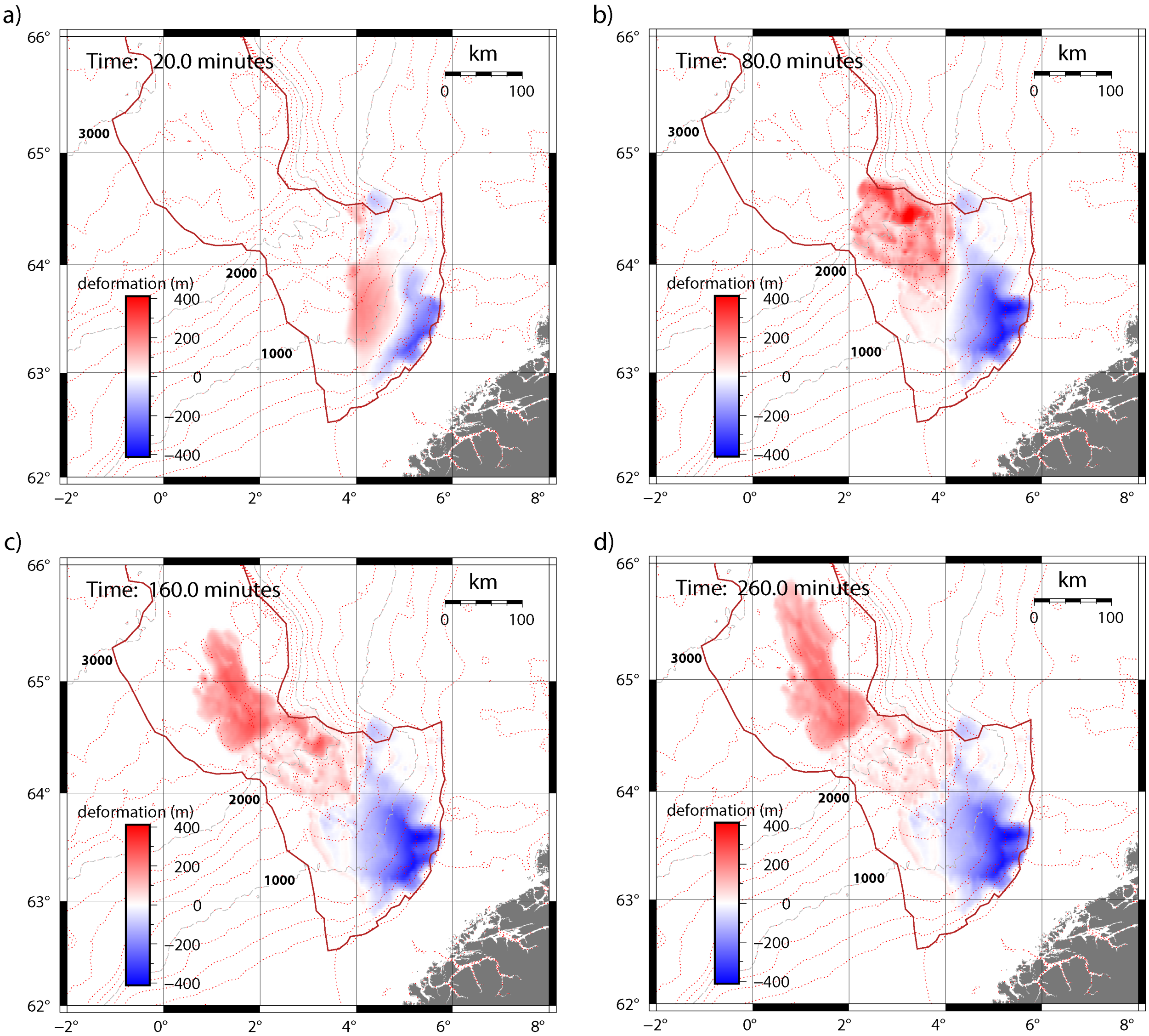

Figure 2: Seafloor deformation relative to the initial bathymetry at (a) 20 minutes, (b) 80 minutes, (c) 160 minutes, and (d) 260 minutes following the slide initiation in a numerical landslide simulation using the BingCLAW code with parameters described by Kim et al. (2019). The thin red dotted contour lines are drawn at 200 meter intervals indicating depth of the initial bathymetry. The contour lines augmented with grey dashes are at 1000 meter intervals and labelled. The solid red line displays the outer boundary of the debris flow sediments from the Storegga slide as indicated by Haflidason et al. (2005).

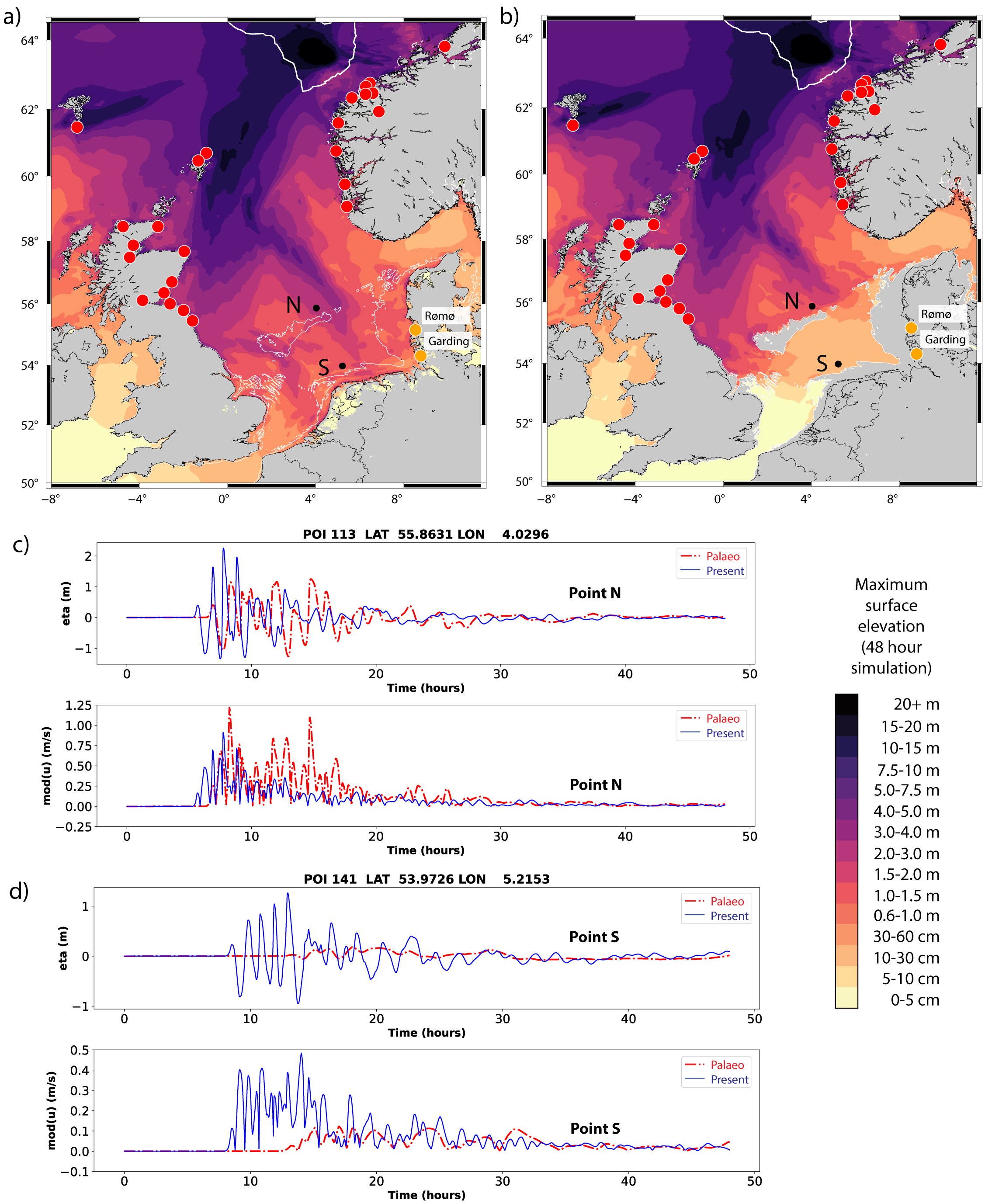

Figure 3: Maximum surface elevation obtained in a numerical tsunami simulation modelling 48 hours of tsunami propagation using (a) contemporary bathymetry and (b) palaeobathymetry (Clark et al., 2022b). Grey indicates land that remained dry throughout the entire duration of the tsunami simulation. The thin white lines indicate the coastline 8000 yr BP after Clark et al. (2022b) for comparison and context and the thin black lines mark the current day coastlines. Panels (c) and (d) display time-series of the surface elevation (eta) and the modulus of velocity (flow speed) for the points labelled N and S respectively. The red symbols mark the locations of Storegga deposits as given by Bondevik (2019). The orange circles mark Rømø, Denmark (8.533°E,55.157°N: Fruergaard et al., 2015b) and Garding, Germany (8.776°E, 54.304°N: Vött et al., 2024). We see that the deposits in the UK, Norway, Shetland, and the Faroes coincide with locations with high modelled tsunami surface elevation. The numbers of the Points of Interest (POIs) indicate the site numbers in the time-series files in the Simulation Data Lake.

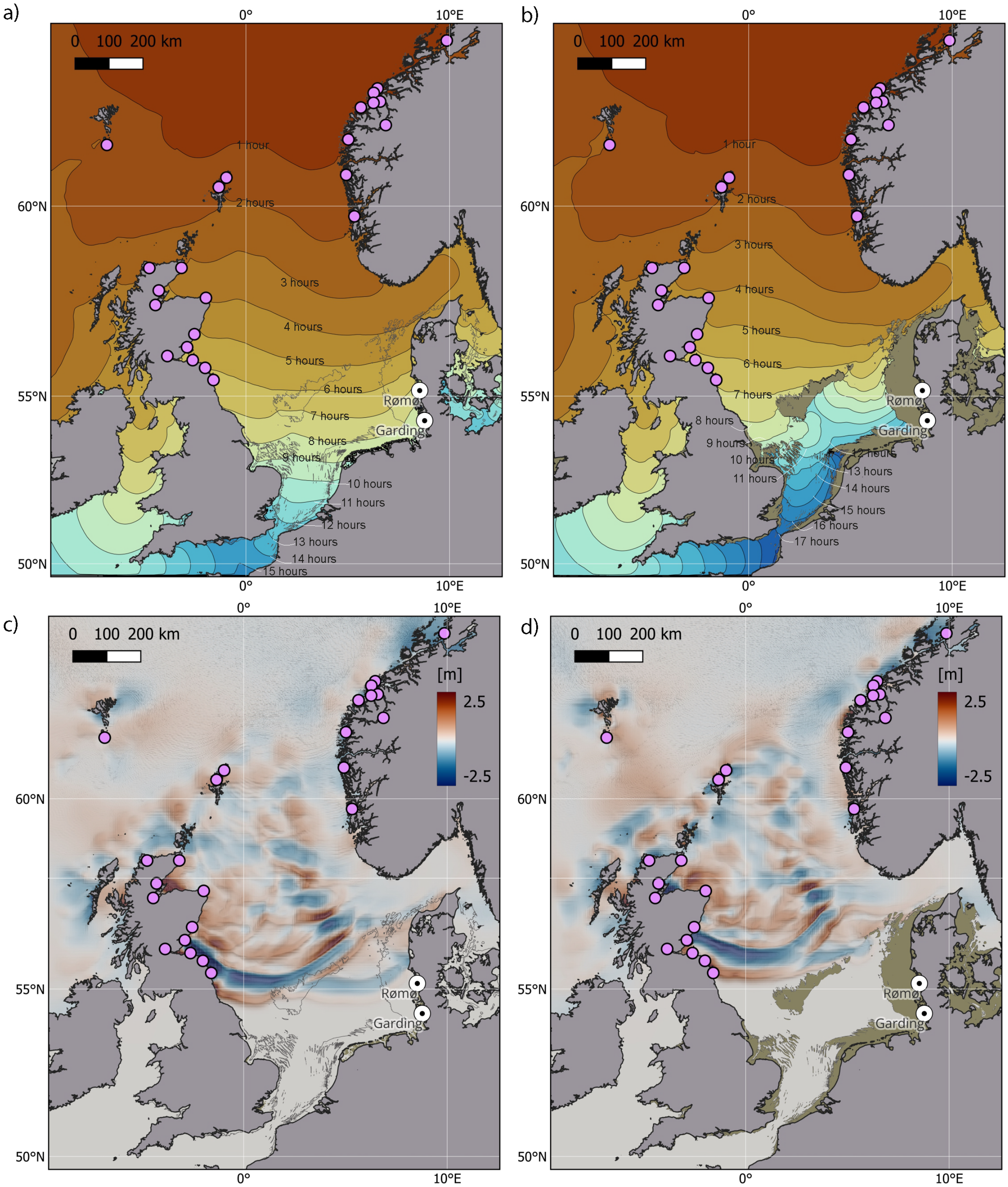

Figure 4: Arrival time in hours of the initial tsunami wave for the two numerical tsunami simulations displayed in Fig. 3 with (a) contemporary bathymetry and (c) the Clark et al. (2022b) palaeobathymetry. Panels (b) and (d) display the surface elevation at 7 hours for the two calculations.

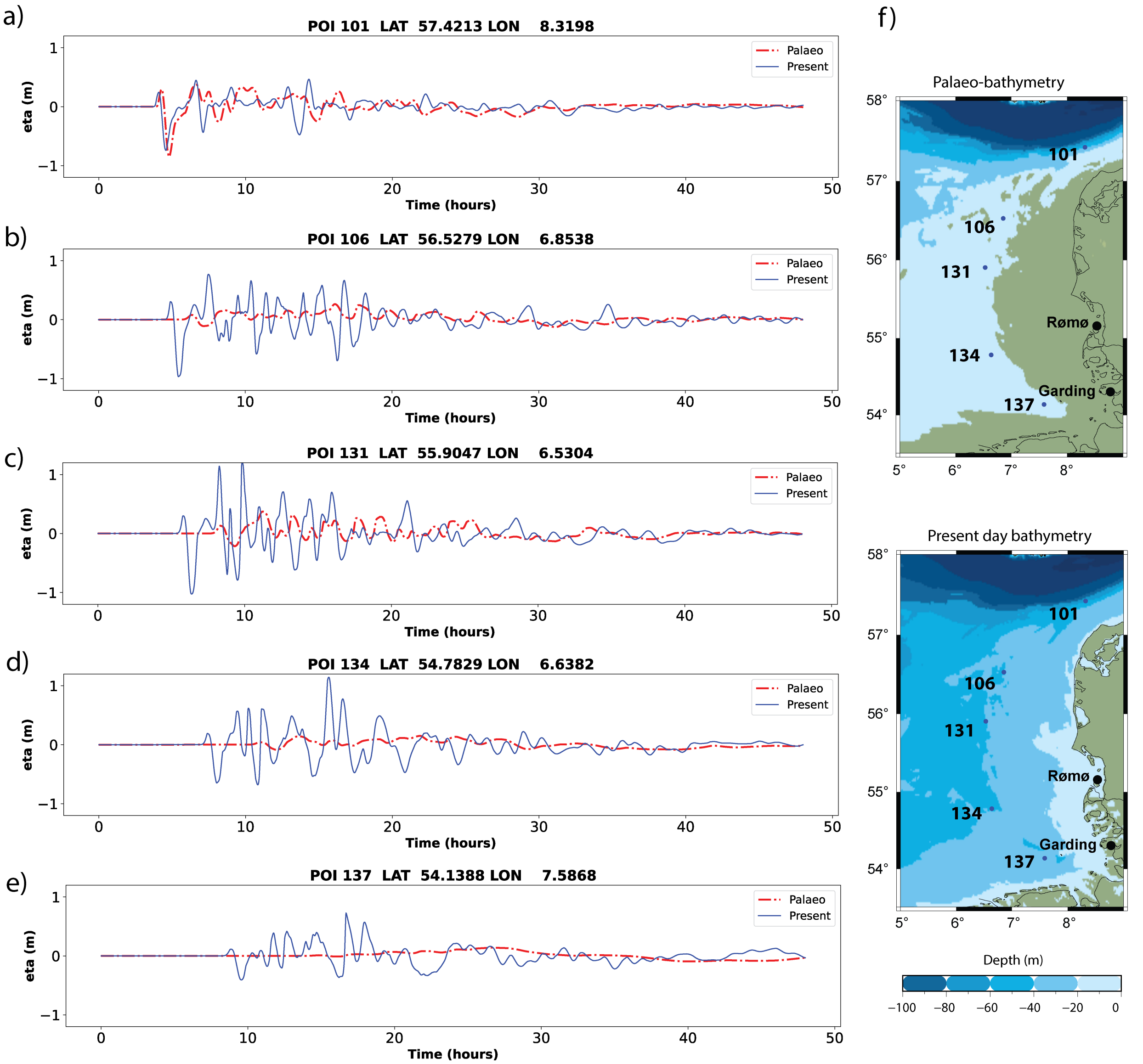

Figure 5: Time-series of surface elevation for both contemporary and palaeobathymetries at five selected locations (panels a-e) following the palaeocoastline of Denmark. Panel (f) contains maps indicating the water depth relative to the locations (Points of Interest, POIs) in the respective models. The palaeobathymetric model of Clark et al. (2022b) is applied here. The numbers of the Points of Interest (POIs) indicate the site numbers in the time-series files in the Simulation Data Lake.

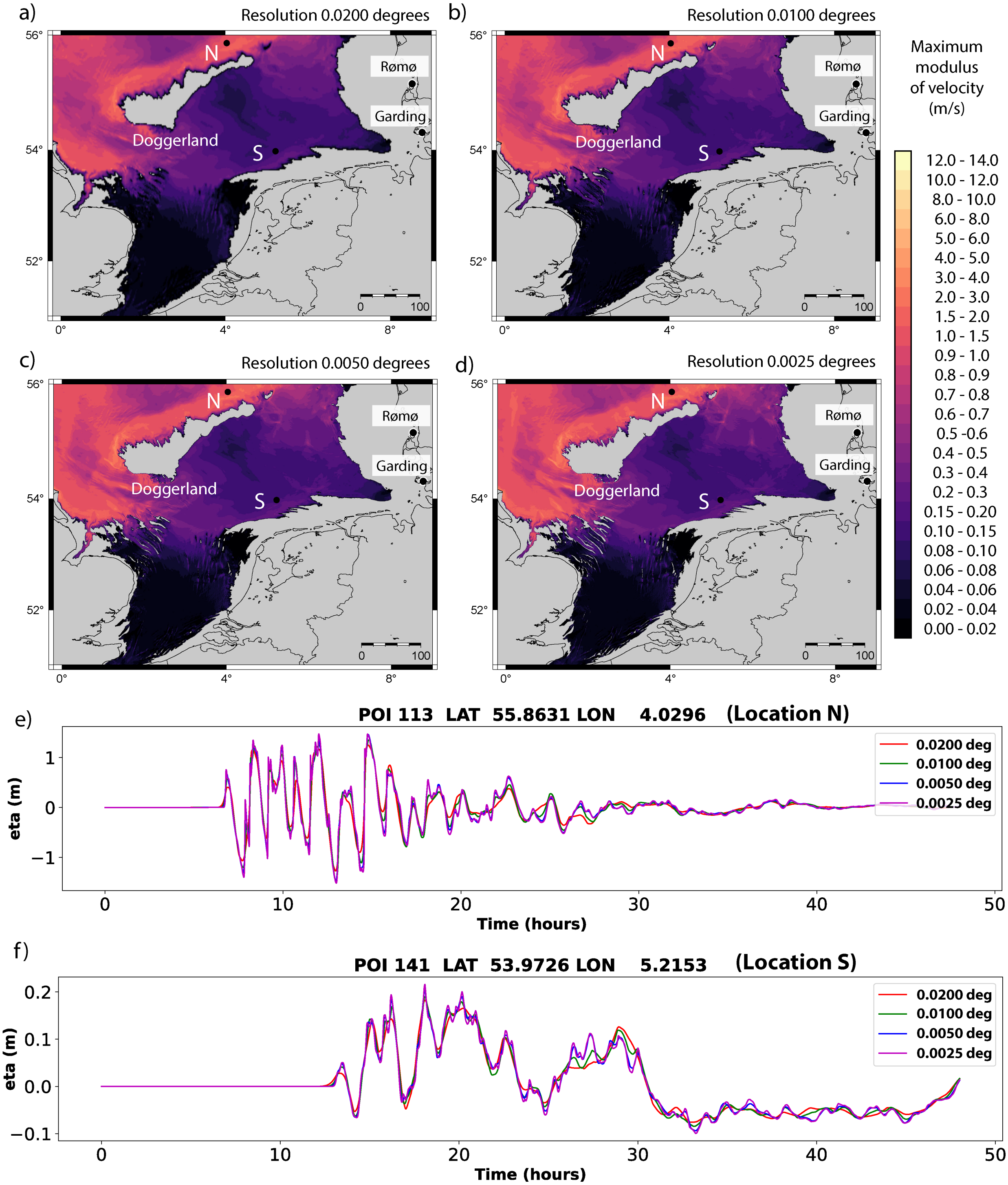

Figure 6: Demonstration of model convergence for simulations with different grid resolutions. Panels (a), (b), (c) and (d) display maximum modulus of velocity (flow speed) for simulations on palaeobathymetry with cell dimensions of $0.02°$, $0.01°$, $0.005°$, and $0.0025°$ respectively. Panels (e) and (f) show time-series of surface elevation at the points labelled N and S for the full duration of the simulation for all spatial resolutions. The palaeobathymetric model of Clark et al. (2022b) is applied here. The numbers of the Points of Interest (POIs) indicate the site numbers in the time-series files in the Simulation Data Lake.

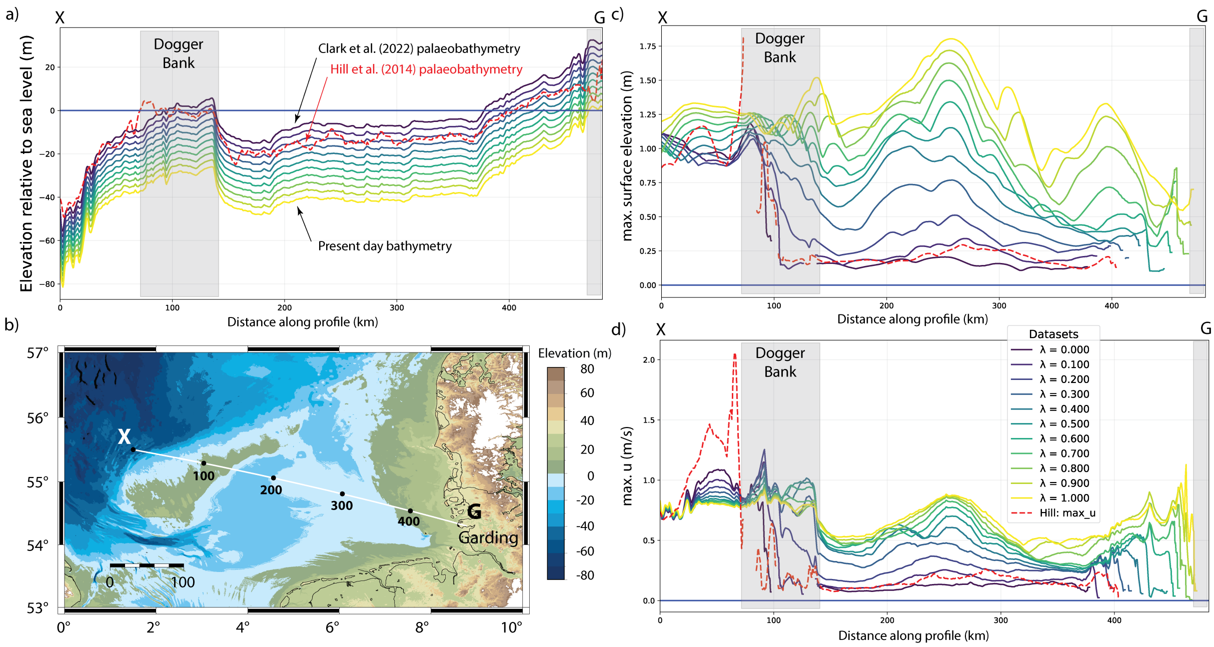

Figure 7: Sensitivity of tsunami metrics to the imposed bathymetry performed using a continuum of bathymetric models between the model of Clark et al. (2022b) ($\lambda = 0$, dark blue) and the present day bathymetry ($\lambda = 1$, yellow). A single calculation for the palaeobathymetric model applied by Hill et al. (2014) is displayed with the red curves. Sections of (a) topographic elevation, (c) max. tsunami surface elevation, and (d) max. modulus of velocity (flow speed) along a profile (displayed in panel b) between points X (55.50°N, 1.50°E) and G (Garding, Germany: 54.33°N, 8.78°E) given the suite of topobathymetric models as indicated. The grey boxes to the left indicate the approximate extent of the regions that are above sea level for some or for all of the models. The grey boxes to the right indicate the part of the profile that is above sea level in the present day topobathymetry (and hence for all models). The numbered black dots along the profile in panel (b) indicate the distance in km from point X and hence correspond to the numbers on the axes in panels a), c), and d).

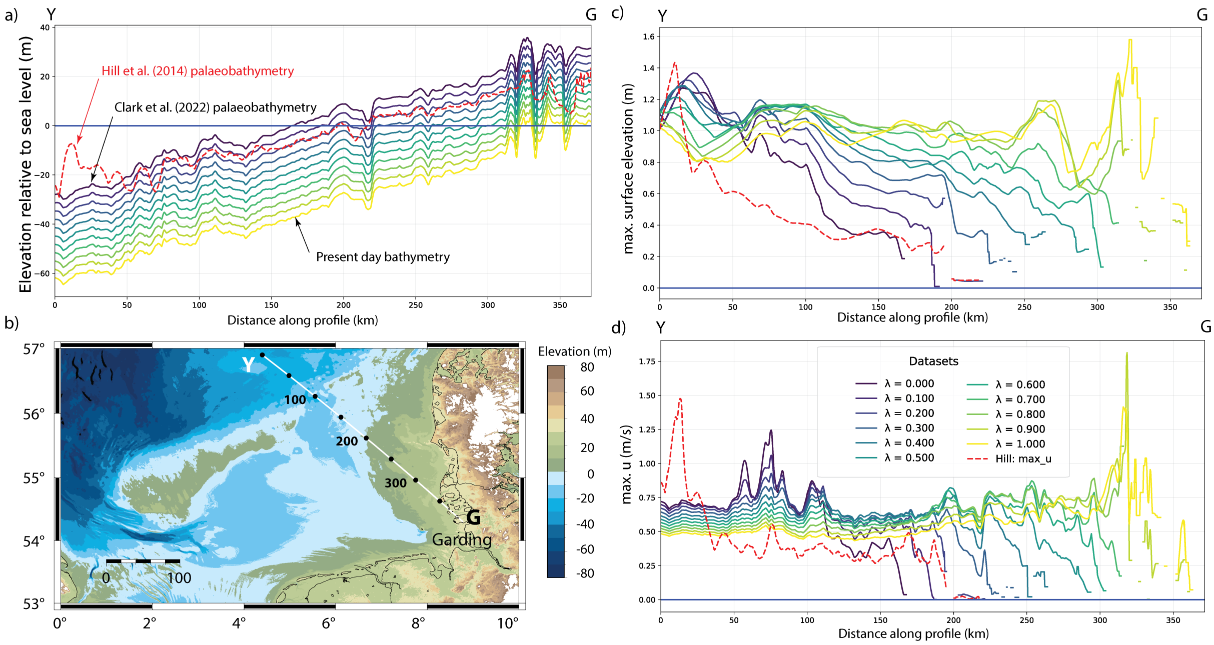

Figure 8: Sensitivity of tsunami metrics to the imposed bathymetry performed using a continuum of bathymetric models between the model of Clark et al. (2022b) ($\lambda = 0$, dark blue) and the present day bathymetry ($\lambda = 1$, yellow). A single calculation for the palaeobathymetric model applied by Hill et al. (2014) is displayed with the red curves. Sections of (a) topographic elevation, (c) max. tsunami surface elevation, and (d) max. modulus of velocity (flow speed) along a profile (displayed in panel b) between points Y (56.90°N, 4.40°E) and G (Garding, Germany: 54.33°N, 8.78°E) given the suite of topobathymetric models as indicated. The black dots along the profile in panel (b) indicate the distance in km from point X and hence correspond to the numbers on the axes in panels a), c), and d).

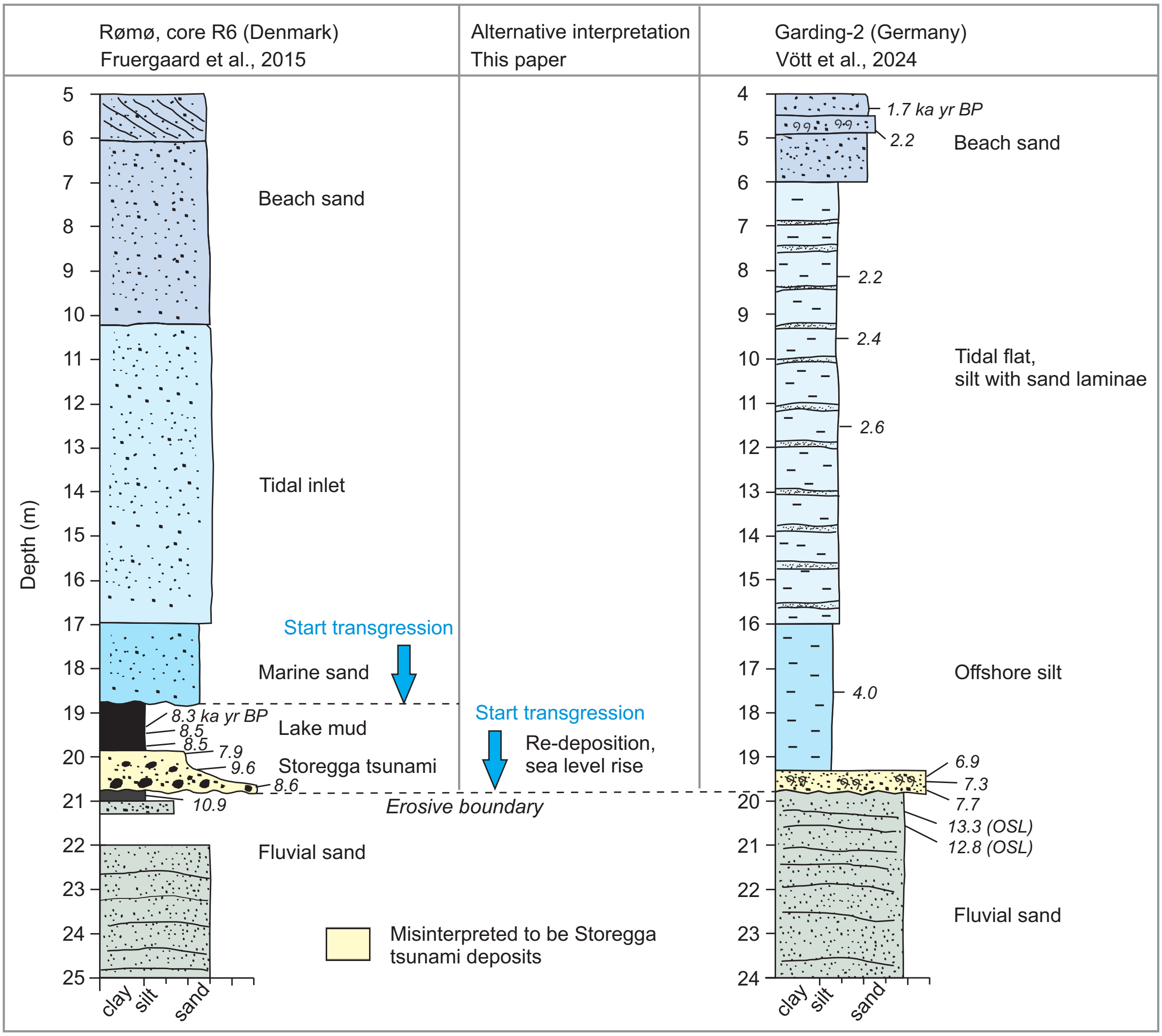

Figure 9: Alternative explanation to the deposits inferred to be Storegga tsunami deposits in Denmark and Germany. Sedimentary logs are redrawn and simplified from the supplement to Fruergaard et al. (2015b) (Rømø, core R6) and from Zhang et al. (2014) (Garding-2). Radiocarbon dates of terrestrial samples are calibrated to IntCal20 (Reimer et al., 2020) and marine samples to Marine 20 (Heaton et al., 2020) using a ΔR value of -19 ± 140yr. These calibrated dates are shown as thousand years BP without standard deviation.